

Measurement of the scintillation resolution in liquid xenon and its impact for future segmented calorimeters

C. Romo-Luque,¹ J.M. Benlloch-Rodríguez,² R. Esteve,³ V. Herrero,³ N. Salor-Iguñiz,²
R.J. Aliaga,⁴ V. Álvarez,³ F. Ballester,³ R. Gadea,³ J. Generowicz,⁵ A. Laing,⁵ F. Monrabal,^{2,6}
M. Querol,¹ M. Rappaport,⁷ J. Rodríguez,³ J. Rodríguez-Ponce,¹ S. Teruel-Pardo,¹
J.F. Toledo,³ R. Torres-Curado,³ P. Ferrario,^{2,6,*} and J.J. Gómez-Cadenas^{2,6,†}

¹*Instituto de Física Corpuscular (IFIC), CSIC & Universitat de València,
Calle Catedrático José Beltrán, 2, Paterna, E-46980, Spain*

²*Donostia International Physics Center, BERC Basque Excellence Research Centre,
Manuel de Lardizabal 4, Donostia-San Sebastián, E-20018, Spain*

³*Instituto de Instrumentación para Imagen Molecular (I3M),
Centro Mixto CSIC - Universitat Politècnica de València, Camino de Vera s/n, Valencia, E-46022, Spain*

⁴*Instituto Universitario de Matemática Pura y Aplicada (IUMPA),*

Universitat Politècnica de València, Camino de Vera s/n, Valencia, E-46022, Spain

⁵*FULL BODY INSIGHT, S.L. Plaza Juan de Ribera 7-A, 46520, Puerto de Sagunto, Spain*

⁶*Ikerbasque (Basque Foundation for Science), Bilbao, E-48009, Spain*

⁷*Weizmann Institute of Science, Herzl St 234, Rehovot, Israel*

(Dated: January 27, 2023)

We report on a new measurement of the energy resolution that can be attained in liquid xenon when recording only the scintillation light. Our setup is optimised to maximise light collection, and uses state-of-the-art, high-PDE, VUV-sensitive silicon photomultipliers. We find a value of $4.2\% \pm 0.2\%$ FWHM at 511 keV, a result much better than previous measurements and close to the Poissonian resolution that we expect in our setup ($5.4\% \pm 0.8\%$ FWHM at 511 keV). Our results are compatible with a null value of the intrinsic energy resolution in liquid xenon, with an upper bound of 0.4% FWHM at 95% CL at 511 keV, to be compared with 3–4% FWHM in the same region found by theoretical estimations which have been standing for the last twenty years. Our work opens new possibilities for apparatus based on liquid xenon and using scintillation only. In particular it suggests that modular scintillation detectors using liquid xenon can be very competitive as building blocks in segmented calorimeters, with applications to nuclear and particle physics as well as Positron Emission Tomography technology.

I. INTRODUCTION

A large number of experiments in nuclear and particle physics require the measurement of energy, position and timing with high resolution. Good energy resolution can be attained with the use of high light-yield materials, while time resolution requires fast decay time. In addition, calorimetry requires high density and good optical quality, e.g., a material transparent to its own emission light.

A number of crystals made of inorganic scintillators offer, to variable degrees, all of the above. Among these, the most extensively used is NaI(Tl), a very bright ($y = 38\,000$ photons/MeV) and fast scintillator ($\tau = 250$ ps). Other popular inorganic scintillators are CsI(Tl) ($y = 17\,100$ photons/MeV, $\tau = 1000$ ps), LYSO(Ce) ($y = 25\,000$ photons/MeV, $\tau = 40$ ps) and BGO ($y = 8\,200$ photons/MeV, $\tau = 300$ ps). The density of the above scintillators vary between 3.7 gr/cm³ (for NaI) and 7.2 gr/cm³ (for LYSO). Good spatial resolution is also often a requirement of nuclear and particle

physics experiments. This can be achieved by segmenting the scintillators (along the transverse plane relative to the incident particles).

All of the above crystals have either been used in, or actively pursued for, high energy and nuclear physics experiments. NaI was used in Crystal Ball, CsI in CLEO and BGO in L3. LYSO is one of the best candidates for future collider applications, due to its excellent properties (high light yield, fast decay time, high density) and radiation hardness [1]. LYSO is also the preferred scintillation material in modern Positron Emission Tomography (PET) scanners[2–4].

The common element in many nuclear and particle calorimeters and in modern PET scanners is a *Segmented Scintillating Block*, SSB (figure 1). An SSB is an array of contiguous cells filled with scintillating material. The light propagates inside each cells by reflection, until it reaches the readout sensor, normally a SiPM in modern devices, although PMTs and APDs were used in the past. The thickness of the cells depends on the application and varies between one and a few radiation lengths. The SSB can be characterised by three parameters: energy resolution, which depends on the scintillator’s light yield, as well as the optical collection efficiency of the cell, the photodetection efficiency (PDE) of the SiPM, electronic noise, etc; time resolution, which is dominated by the

* Corresponding author.; paola.ferrario@dipc.org

† Corresponding author.; jjgomezcadenas@dipc.org

scintillator's decay time; and (transverse) spatial resolution, which can be tailored by choosing a suitable transverse size for the cell. As an example, in the 2 m long EXPLORER scanner [5, 6], the largest reported PET, the SSB material is LYSO, with cell area $2.76 \times 2.76 \text{ mm}^2$ and thickness of 1.6 radiation lengths, and the cells are read out by SiPMs. The number of individual cells exceeds 500 000. The energy resolution at 511 keV is 12% FWHM, the spatial resolution $\sim 3 \text{ mm}$ and the time-of-flight (TOF) resolution is 500 ps.

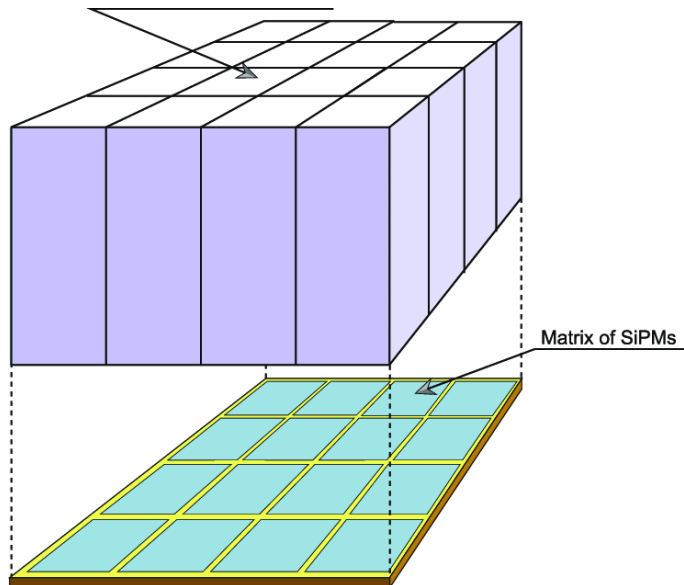


FIG. 1. A schematic illustrating the concept of SSB.

Liquid xenon (LXe) is also an excellent calorimeter [7]. Charged particles interact with LXe via both ionisation and excitation. The excitation of xenon atoms results in strongly bound excited molecules (excimers) which, on de-excitation, emit VUV photons with a wavelength of $\sim 175 \text{ nm}$ [8]. In addition, the xenon atoms are ionised. An external electric field can be used to carry away the ionisation electrons, in which case two signals are available, one from scintillation, and one from ionisation. In the absence of such electric field, most ionisation electrons eventually recombine with positive xenon ions, and both channels (primary scintillation and recombination) contribute to the resulting scintillation yield, $\sim 58\,700$ photons per MeV [9], which is a factor 1.5 larger than NaI and 1.7 larger than LYSO. Several measurements have found yield fractions of primary scintillation and recombination of roughly 0.25 and 0.75 [9]. The primary scintillation is characterised by two decay constants ($\tau_1 = 3 \text{ ps}$, $\tau_2 = 27 \text{ ps}$), while the decay time associated with recombination is $\tau_3 = 40 \text{ ps}$. Thus, LXe is, *a priori*, a brighter and (slightly) faster scintillator than LYSO. However, its radiation length is almost three times longer than that of LYSO and the fraction of photons which interact via the photoelectric effect (relevant for PET application) a factor of two less.

LXe has been used extensively in particle physics and astronomy. In particular, the MEG experiment [10] deployed a large calorimeter—800 litres volume filled with LXe—, with a thickness of 17 radiation lengths and read out by 846 $2''$ UV-sensitive photomultiplier tubes. Other important examples are experiments searching for rare events, in particular neutrinoless double beta decay [11] and direct Dark Matter searches [7, 9]. Future experiments such as nEXO [12] and DARWIN [13] are also based on LXe. All these detectors are Time Projection Chambers, able to read the scintillation and ionisation signals in LXe. Since the energy deposited by ionising particles is distributed between both channels, the anti-correlation of the signals leads to a good energy resolution. For example, the EXO-200 experiment measures 2.9% FWHM at 2.6 MeV [14].

The possibility of building a PET scanner based on LXe was proposed more than four decades ago [15] and explored by a number of subsequent works [16–19]. Two strategies were considered: a PET scanner based on scintillation only, and one that would combine both ionisation and scintillation. Given the very high rate of PET scans, the second strategy may be unpractical, due to the long time (microseconds) needed to drift the charge. The LXe micro-PET prototype obtained an energy resolution of 10% FWHM [19] combining scintillation and charge, while the XEMIS1 prototype measured 9% FWHM [20] with charge only. On the other hand, several groups tried prototypes based on pure scintillation (measured by PMTs), obtaining an energy resolution of 15–26% FWHM [18, 21]. None of these results were compelling enough to consider LXe as a viable alternative to standard inorganic crystals, in particular LYSO. Recently, the possibility of building a LXe-PET using modern SiPM technology (thus providing better energy resolution and time-of-flight than that possible in the past) has been considered by our group [22–27].

In order to assess the potential of LXe as calorimetric medium, in particular when using only scintillation light, it is essential to understand its intrinsic energy resolution (R_i). The intrinsic resolution of a scintillator refers to the fundamental limit at which Poisson statistics does not improve resolution due to underlying physics. For example, the energy resolution of NaI(Tl), which, as mentioned above, is the most popular inorganic scintillator, is much worse than that expected from Poisson statistics in the energy region of MeV, thus partially spoiling its suitability for PET. The underlying physics explanation is the non-proportionality of the scintillation yield in NaI(Tl) for secondary electrons.

In 2002, Doke studied the intrinsic energy resolution of LXe [28] and found that non-proportionality of the scintillation yield resulted in $R_i \sim 4\%$ FWHM in the region between 100 keV and $\sim 5 \text{ MeV}$ (figure 2). His calculation is in good agreement with the modern Monte Carlo code describing the physics of LXe, NEST [29]. Specifically, at 511 keV, NEST predicts $R_i \sim 3\%$ FWHM. Instead, Ni and collaborators found in 2006 an intrinsic energy reso-

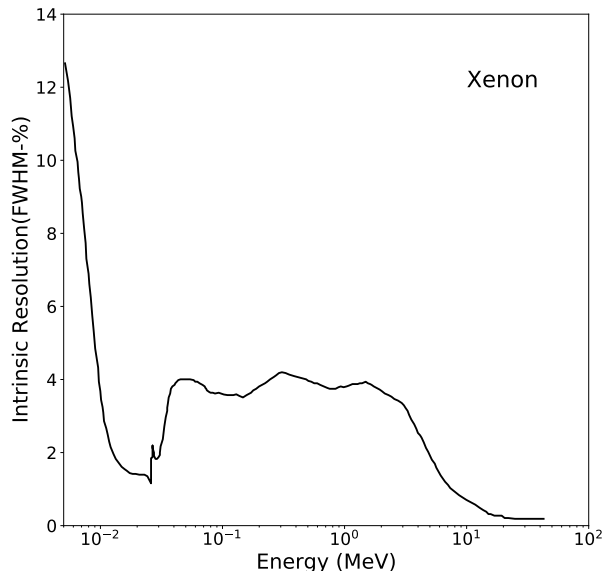


FIG. 2. Intrinsic energy resolution in LXe. Reproduced from Ref. [28].

lution of 14% FWHM [30], almost a factor ~ 5 worse than Doke’s (and NEST) estimations. To our knowledge, this discrepancy has not been resolved to date. These results, as well as previous works by Doke and Chepel [16, 18], effectively excluded xenon as a competitive scintillator for PET scanners.

In this paper, we present a new measurement of the energy resolution in LXe, using scintillation only. Our setup is conceptually identical to the SSB described above, and illustrated in figure 1, where the scintillating material is now LXe. The advantage of the SSB is its large light collection efficiency, as well as the availability of VUV-SiPMs with large PDE. This results in a large number of detected photoelectrons, thus minimising Poisson fluctuations and leading to a measurement close to R_i .

On the other hand, we have seen that SSBs based on a variety of inorganic scintillators constitute the building blocks of calorimeters that have been used or are planned for future experiments in nuclear and particle physics, as well as the basic building block for PETs. The obvious question, then, is whether an SSB based on LXe could be a viable alternative for some of the future applications, and in particular for LYSO blocks in PET applications.

II. SETUP

Our setup, shown schematically in figure 3, consists, conceptually, of two LXe SSBs. A ^{22}Na calibration source, located between the two SSBs, provides pairs of (almost) back-to-back gammas with an energy of 511

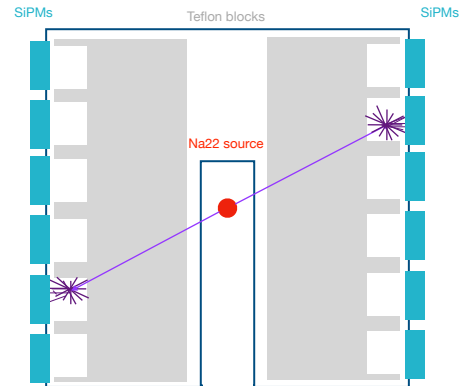


FIG. 3. A schematic view of our experimental setup (not to scale).

keV. Some of the gammas interact in the xenon volume, producing VUV light, which propagates inside the channel in which the interaction occurs. A large fraction of this light reaches the SiPM that (almost) closes the channel. Each SiPM, therefore, provides an independent measurement of the ^{22}Na spectrum. Fitting the region close to the photopeak provides a measurement of the energy resolution, R_m .

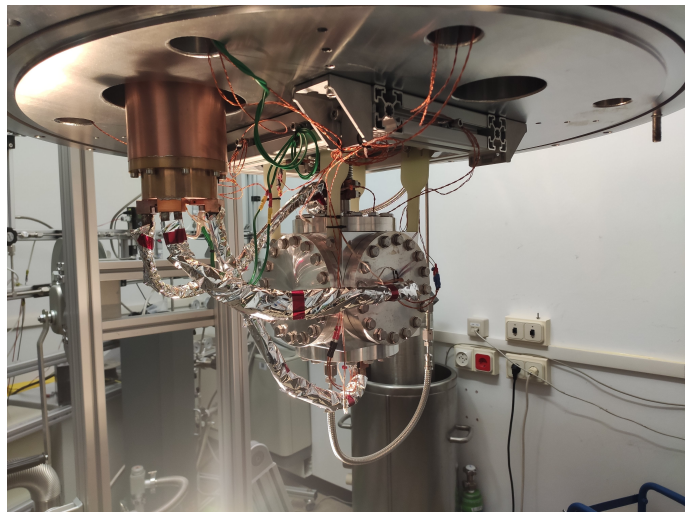


FIG. 4. The aluminum cube holding the two SSBs used for the measurement. Notice the thermal links attached to the cold head.

The active region of the setup consists of two LXe SSBs housed in a metal-sealed aluminum cube (F100-1ALU) from Vacum. The xenon is continuously recirculated in gas phase by a double diaphragm compressor and flows through a model PS4 MT15 R2 hot getter from Sigma Technologies. This process removes nitrogen, oxygen and

water from the xenon, all of which quench xenon scintillation light [31]. The internal cube is housed within a large vacuum vessel so that the structure is thermally isolated while cooled. Said cooling is performed using a Sumitomo CH-110 cold head coupled to the cube via custom-made copper thermal links. Heat dissipation from the thermal links is minimised by wrapping them in polyethylene terephthalate foil. The cube and cooling machinery is visible in figure 4. The gas passes through a heat exchanger when entering and exiting the inner cube, which precools the gas before liquefaction for operation at -109°C and 1.26 bar.

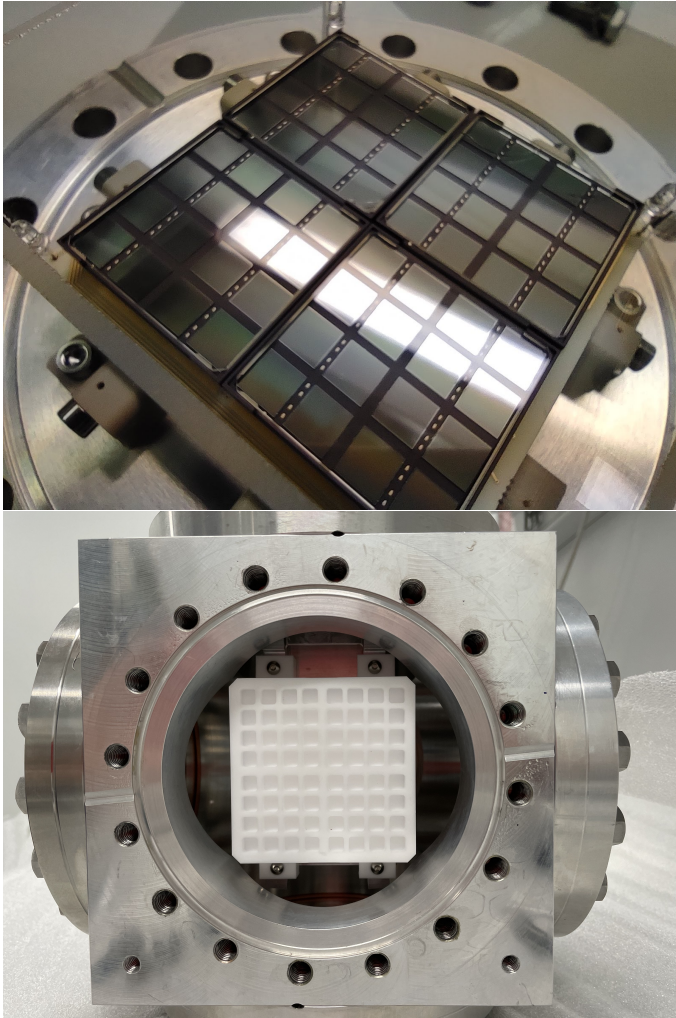


FIG. 5. Top: instrumented plane of four arrays of 4×4 SiPMs. Bottom: teflon piece defining the SSB.

Figure 5 shows the main components of the SSB before mounting and filling with xenon. Figure 5-top shows an array of Hamamatsu S15779(ES1), VUV-sensitive SiPMs. They have 30% photodetection efficiency at the peak wavelength of xenon scintillation and are protected by a quartz window with $\geq 90\%$ transmission at relevant wavelengths. Their active area is $5.95 \times 5.85 \text{ mm}^2$ and they are packed in arrays of 4×4 sensors. Each SiPM

reads out a $6 \times 6 \text{ mm}^2$, 5-mm deep hole in a polytetrafluoroethylene (PTFE) piece (figure 5-bottom). The two SSBs are mounted inside the aluminum cube with the sensitive face of the SiPMs facing each other. The teflon pieces are mounted to leave a 0.5 mm gap between the SiPM face and the end of the empty cell. In this way the LXe can easily fill the gaps, completing the SSB cells. The result is that each SiPM is exposed to the scintillation light of gamma interactions occurring only in the hole in front of it. The high reflectivity of the PTFE at VUV wavelengths ($\sim 98\%$) [32, 33] ensures a high geometric light collection efficiency.

Signals are digitized using two TOFPET2 ASICs [24, 34], one for each read-out plane, mounted in vacuum on the outside walls of the cube corresponding to the relevant SiPM array. They integrate detected charge and provide a fast timestamp close to origin to reduce signal degradation before digitization.

Welded to the bottom flange of the cube is a rectangular aluminum calibration port, sealed at the top end and extending above the center of the cube. This allows the insertion of sources between the two SSBs for coincidence measurements using back-to-back gammas. For the measurements reported here, a ^{22}Na calibration source is placed in the center of the cube inside the calibration port. The radioactive material (with an activity of $\sim 330 \text{ kBq}$) is a sphere of 0.25 mm diameter, which can be considered point-like, and is encapsulated in a plastic support.

III. MEASUREMENT

During a run, a timestamp is provided by the ASIC whenever the recorded charge exceeds a lower threshold in a channel; if the charge exceeds a second, higher threshold, the ASIC starts integrating it, until it goes below the higher threshold again. If the second threshold is not reached, the integrated charge is not saved.

The output of the data acquisition is, therefore, a list of channels with an integrated charge and a timestamp. Once the channels are divided event by event, a first filter is applied to retain only coincidences, i.e., events where (at least) one sensor from each detection plane is present. Given the cell-structure of the SSBs, most of the charge is read out by the sensor coupled to the xenon volume where the interaction happened, therefore we single out the sensor with larger detected charge for each plane.

Figure 6 shows the photoelectric peak, together with the Compton shoulder for one of the channels. A normal distribution is fitted to a region around the peak to extract the resolution. To choose the region, we vary the range to the left and to the right of the photopeak, until the fit χ^2 starts to worsen showing that the data is no longer described by a gaussian. We keep the pair of range values that gives the minimum and maximum value of the resolution, defined as

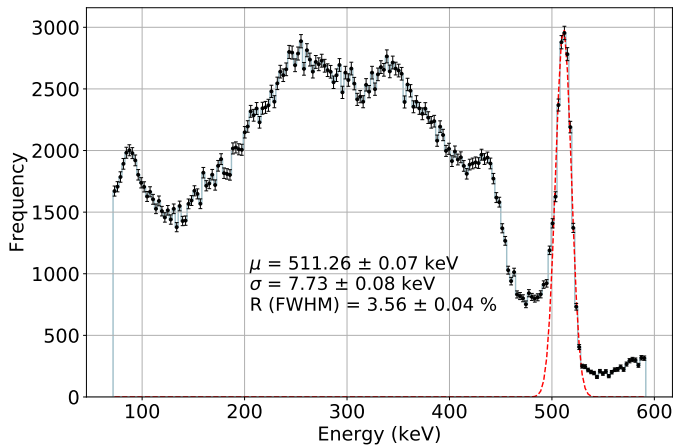


FIG. 6. Distribution of the charge detected by one of the SiPMs, fitted to a normal function in the photo-peak. The fit extends until the region where the data is no longer gaussian.

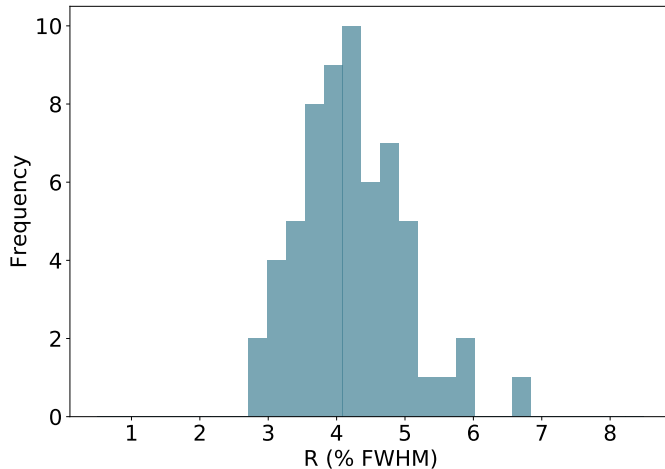


FIG. 7. Distribution of the resolution measured in each cell in the reference plane.

$$R = 2.35 \times \frac{\sigma}{\mu} \quad (1)$$

with σ and μ the best values for the gaussian parameters coming from the fit. The central value is calculated as $R_{\text{cent}} = (R_{\text{max}} + R_{\text{min}})/2$. The same procedure is applied to all the sensors in the SSB.

Figure 7 shows the distribution of the central values of the resolution for the SiPMs of the reference SSB used in the measurement. The reason for choosing only one SSB is that one SSB is aligned better than the other and the response of the sensors is more uniform. We calculate the error of the measurement, given by the error of the fit procedure, averaging the maximum and minimum values of the resolution over all the sensors, according to $R_{\text{err}} = (R_{\text{max}}^{\text{ave}} - R_{\text{min}}^{\text{ave}})/2$, where $R_{\text{max}}^{\text{ave}}$ is the average of the maximum (minimum) resolutions extracted from the fit,

over all the sensors. We find a systematic error of 0.2% FWHM. The central value, given by $(R_{\text{max}}^{\text{ave}} + R_{\text{min}}^{\text{ave}})/2$, is 4.2% FWHM. Therefore, the result of our measurement is $4.2\% \pm 0.2\%$ FWHM.

IV. RESULTS

Following Doke [28], the measured resolution, R_m , can be seen as the quadratic sum of the intrinsic resolution, R_i , and the resolution due to Poisson variation in photon detection, as shown in Eq. 2:

$$R_m^2 = R_i^2 + R_p^2. \quad (2)$$

The latter term combines contributions from the scintillation process, the reflections on PTFE and on the quartz windows in front of the SiPMs, geometric acceptance, sensor PDE and the amplification stages of the electronics.

To calculate the resolution associated with Poisson fluctuations we use a Monte Carlo software application based on GEANT4 [35]. We simulate the decay of a ^{22}Na source in a geometry that represents our setup. The physical and optical properties of the materials in use are simulated in detail, in particular the reflectivity of PTFE, which has been modelled as a Lambertian reflectivity with a value of 98%. The other physical parameters relevant for optical photon propagation are the Rayleigh scattering length (36 cm [36]) and the transparency and refractive index of the quartz window placed in front of the SiPMs to protect them (90% and 1.6, respectively). The photodetection efficiency provided by the sensor datasheet is also included as a function of the wavelength of the optical photons. We turn off any intrinsic fluctuation of the LXe response to gamma interactions, so that the amount of scintillation photons produced is proportional to the deposited energy. We analyze the simulated data in the same way as real data and we obtain a resolution of $R_p = 5.4\% \pm 0.8\%$ FWHM. Since no intrinsic fluctuations are present, the only contribution to this resolution is Poisson variation in photon detection. The error includes the uncertainties in the optical modelling of Monte Carlo, such as the reflectivity of teflon and the reflection and refraction between LXe and the quartz window that protects the SiPMs.

Using Eq. 2, we can conclude that this result is compatible with a null value of R_i within errors, meaning $R_m = R_p$. An upper limit to the intrinsic resolution of LXe can be set in the following way. Random numbers are generated following two gaussian distributions, g_m and g_p , with mean and sigma values equal to those of R_m ($g_m(4.2, 0.2)$) and R_p ($g_p(5.4, 0.8)$). We calculate the upper limit on R_i as:

$$R_i^{\text{up}} = \mu_{\text{diff}} + 1.96 \times \sigma_{\text{diff}} \quad (3)$$

where μ_{diff} and σ_{diff} are the mean and standard deviation of the distribution resulting from $g_m - g_p$. Therefore,

we find that the intrinsic resolution of LXe is lower than 0.4% FWHM at 95% confidence level.

V. DISCUSSION

In this work, we have measured the resolution that can be attained in a segmented scintillation block (SSB) filled with LXe and read out by VUV-SiPMs. The SSB was designed to have large acceptance and the SiPMs have the largest PDE currently available in the market. The intrinsic resolution that our procedure yields is compatible with zero, with an upper value (at 95% CL) of 0.4% FWHM. Previous measurements of the intrinsic resolution yielded very high values (14% FWHM), not compatible with our current measurement. Our result also questions the notion that there is an intrinsic resolution at all associated to scintillation in liquid xenon, as proposed by [28].

Furthermore, our work opens new possibilities for apparatus using liquid xenon scintillators and scintillation only. In particular it suggests that SSBs using LXe as a scintillator can be very competitive as building blocks in segmented calorimeters, with applications to nuclear and particle physics as well as PET technology. While there is ample room for technological development (maximising the light collection efficiency of the SSB and eventually increasing the PDE of the SiPMs), our measurement clearly suggests that a LXe-SSB can compete and eventually outperform, in terms of energy resolution, those using other scintillators.

ACKNOWLEDGMENTS

This work was supported by the European Research Council under grant ID 757829.

-
- [1] M. Yeh and R.-Y. Zhu, Materials for future calorimeters (2022).
- [2] S. Vandeberghe, P. Moskal, and J. Karp, State of the art in total body pet, *EJNMMI Physics* **7**, 35 (2020).
- [3] V. Westerwoudt, M. Conti, and L. Eriksson, Advantages of improved time resolution for TOF PET at very low statistics, *IEEE Trans. Nucl. Sci.* **61**, 126 (2014).
- [4] M. Conti and B. Bendriem, The new opportunities for high time resolution clinical TOF PET, *Clinical and Translational Imaging* **7**, 139 (2019).
- [5] S. R. Cherry *et al.*, Total-body PET: Maximizing sensitivity to create new opportunities for clinical research and patient care, *J. Nucl. Med.* **59**, 3 (2018).
- [6] R. D. Badawi *et al.*, First human imaging studies with the EXPLORER total-body PET scanner, *J. Nucl. Med.* **60**, 299 (2019).
- [7] E. Aprile and T. Doke, Liquid xenon detectors for particle physics and astrophysics, *Rev. Mod. Phys.* **82**, 2053 (2010), arXiv:1207.2292 [physics.ins-det].
- [8] K. Fujii *et al.*, High-accuracy measurement of the emission spectrum of liquid xenon in the vacuum ultraviolet region, *Nuclear Instruments and Methods in Physics Research Section A: Accelerators, Spectrometers, Detectors and Associated Equipment* **795**, 293 (2015).
- [9] V. Chepel and H. Araujo, Liquid noble gas detectors for low energy particle physics, *JINST* **8**, R04001, arXiv:1207.2292 [physics.ins-det].
- [10] G. Gallucci, The meg liquid xenon calorimeter, *Journal of Physics: Conference Series* **160**, 012011 (2009).
- [11] G. Anton *et al.* (EXO-200 Collaboration), Search for neutrinoless double- β decay with the complete exo-200 dataset, *Phys. Rev. Lett.* **123**, 161802 (2019).
- [12] G. Adhikari *et al.*, *Journal of Physics G: Nuclear and Particle Physics* **49**, 015104 (2021).
- [13] J. Aalbers *et al.*, DARWIN: towards the ultimate dark matter detector, *Journal of Cosmology and Astroparticle Physics* **2016** (11), 017.
- [14] G. Anton *et al.*, Measurement of the scintillation and ionization response of liquid xenon at MeV energies in the EXO-200 experiment, *Physical Review C* **101**, 10.1103/physrevc.101.065501 (2020).
- [15] L. Lavoie, Liquid xenon scintillators for imaging of positron emitters, *Med. Phys.* **3** (5), 283 (1976).
- [16] V. Chepel *et al.*, The liquid xenon detector for PET: recent results, *IEEE Transactions on Nuclear Science* **NS-46**, 1038 (1999).
- [17] P. Crespo *et al.*, Pulse processing for the PET liquid xenon Multiwire Ionisation Chamber, *IEEE Transactions on Nuclear Science* **47**, 2119 (1999).
- [18] T. Doke, J. Kikuchi, and F. Nishikido, Time-of-flight positron emission tomography using liquid xenon scintillation, *Nucl. Instrum. Methods A* **569**, 863 (2006).
- [19] A. Miceli, Liquid xenon detectors for positron emission tomography, *J. Phys. Conf. Ser.* **312**, 062006 (2011).
- [20] Y. Z. ane others, Studies and optimization of scintillation light measurements for the development of the 3-gamma medical imaging xemis2 liquid xenon compton camera, *Nuclear Instruments and Methods in Physics Research Section A: Accelerators, Spectrometers, Detectors and Associated Equipment* , 167794 (2022).
- [21] V. Chepel, Liquid xenon detectors for medical imaging, *Revista do Detua* **4** (2007).
- [22] J. J. Gomez-Cadenas *et al.*, Investigation of the Coincidence Resolving Time performance of a PET scanner based on liquid xenon: A Monte Carlo study, *JINST* **11** (09), P09011, arXiv:1604.04106 [physics.ins-det].
- [23] J. J. Gomez-Cadenas, J. M. Benlloch-Rodríguez, and P. Ferrario, Monte Carlo study of the Coincidence Resolving Time of a liquid xenon PET scanner, using Cherenkov radiation, *JINST* **12** (08), P08023, arXiv:1706.07629 [physics.ins-det].
- [24] V. Herrero-Bosch *et al.*, PETALO read-out: A novel approach for data acquisition systems in PET applications, in *2018 IEEE Nuclear Science Symposium and Medical Imaging Conference (NSS/MIC)* (2018).
- [25] J. Renner *et al.*, Processing of Compton events in the PETALO readout system, in *2019 IEEE Nuclear Science Symposium (NSS) and Medical Imaging Conference*

- (*MIC*) (2019) pp. 1–7, arXiv:2001.04724 [physics.ins-det].
- [26] P. Ferrario *et al.*, PETALO: Time-of-Flight PET with liquid xenon, in *2018 IEEE Nuclear Science Symposium and Medical Imaging Conference (NSS/MIC)* (2018) arXiv:1911.10994 [physics.ins-det].
- [27] J. Renner *et al.*, Monte carlo characterization of PETALO, a full-body liquid xenon-based PET detector, *Journal of Instrumentation* **17**, P05044.
- [28] T. Doke, R. Sawada, and H. Tawara, Non-proportionality of the scintillation yield in liquid xenon and its effect on the energy resolution for gamma-rays, *Technique and Application of Xenon Detectors*, 17 (2003).
- [29] M. Szydagis *et al.*, Noble element simulation technique v2.0 (version v2.0.0), Zenodo 10.5281/zenodo.1314669 (2018).
- [30] K. Ni *et al.*, Gamma Ray Spectroscopy with Scintillation Light in Liquid Xenon, *JINST* **1**, P09004, arXiv:physics/0608034 [physics].
- [31] A. Baldini *et al.*, Absorption of scintillation light in a 100 l liquid xenon gamma-ray detector and expected detector performance, *Nuclear Instruments and Methods in Physics Research Section A* **545**, 753 (2005).
- [32] D. Akerib *et al.*, Technical results from the surface run of the lux dark matter experiment, *Astroparticle Physics* **45**, 34 (2013).
- [33] M. Yamashita *et al.*, Scintillation response of liquid xe surrounded by ptfе reflector for gamma rays, *Nuclear Instruments and Methods in Physics Research Section A: Accelerators, Spectrometers, Detectors and Associated Equipment* **535**, 692 (2004).
- [34] A. Di Francesco *et al.*, Tofpet2: a high- performance asic for time and amplitude measurements of sipm signals in time-of-flight applications, *JINST* **11** (3), C03042.
- [35] S. Agostinelli *et al.*, GEANT4 - a simulation toolkit, *Nucl. Instrum. Meth. A* **506**, 250 (2003).
- [36] V. Solovov *et al.*, Measurement of the refractive index and attenuation length of liquid xenon for its scintillation light, *Nucl. Instrum. Meth. A* **516**, 462 (2004).